

Three-Dimensional Dirac Phonons with Inversion SymmetryZ. J. Chen^{1,2,3}, R. Wang⁴, B. W. Xia^{2,3}, B. B. Zheng², Y. J. Jin^{2,3}, Yu-Jun Zhao^{1,*} and H. Xu^{1,2,3,†}¹*Department of Physics, South China University of Technology, Guangzhou 510640, People's Republic of China*²*Department of Physics and Institute for Quantum Science and Engineering, Southern University of Science and Technology, Shenzhen 518055, People's Republic of China*³*Guangdong Provincial Key Laboratory of Computational Science and Material Design, Southern University of Science and Technology, Shenzhen 518055, People's Republic of China*⁴*Institute for Structure and Function and Department of Physics and Center for Quantum Materials and Devices, Chongqing University, Chongqing 400044, People's Republic of China* (Received 18 December 2019; revised 23 May 2020; accepted 5 April 2021; published 5 May 2021)

Dirac semimetals associated with bulk Dirac fermions are well known in topological electronic systems. In sharp contrast, three-dimensional (3D) Dirac phonons in crystalline solids are still unavailable. Here we perform symmetry arguments and first-principles calculations to systematically investigate 3D Dirac phonons in all space groups with inversion symmetry. The results show that there are two categories of 3D Dirac phonons depending on their protection mechanisms and positions in momentum space. The first category originates from the four-dimensional irreducible representations at the high symmetry points. The second category arises from the phonon branch inversion, and the symmetry guarantees Dirac points to be located along the high symmetry lines. Furthermore, we reveal that nonsymmorphic symmetries and the combination of inversion and time-reversal symmetries play essential roles in the emergence of 3D Dirac phonons. Our work not only offers a comprehensive understanding of 3D Dirac phonons but also provides significant guidance for exploring Dirac bosons in both phononic and photonic systems.

DOI: [10.1103/PhysRevLett.126.185301](https://doi.org/10.1103/PhysRevLett.126.185301)

Recently, various topological phases in condensed matter physics have become the subject of intense studies in electronic systems. These topological phases are associated with specific symmetries, leading to unique nontrivial surface states. For instance, the time-reversal (\mathcal{T}) symmetry guarantees the helical surface states with a Dirac linear dispersion in topological insulators [1,2]. Such features have been identified to be robust against nonmagnetic perturbations, facilitating potential applications in dissipationless devices [2]. Subsequently, the concept of band topology was introduced to semimetals [3], i.e., topological semimetals, which further extend the classification of topological matter. So far, different types of topological semimetals have been theoretically proposed [3–9]. In particular, three-dimensional (3D) Dirac semimetals, in which the low-energy excitations around fourfold-degenerate Dirac points linearly disperse along all momentum directions, have attracted much attention, as they are regarded as 3D analogs of graphene [6–9]. Delightfully, 3D Dirac semimetals have already been experimentally confirmed in Na_3Bi and Cd_3As_2 [10–13].

In comparison with fermionic electrons, bosonic systems possess similar but different properties. On the one hand, bosons do not obey the Pauli exclusion principle. As a result, their topological features are effective in the whole energy range. On the other hand, the spinless Bloch functions in bosonic systems are invariant under an even number of \mathcal{T}

operations, i.e., $\mathcal{T}^2 = 1$ [14]. Such unique features may supply various fascinating properties and potential applications to the family of topological quantum phases. To date, research progress in topological bosons has focused mainly on the artificial photonic [15,16] and phononic [17–20] crystals. Studies of topological phonons in crystalline solids are still in their infancy [21–27]. In particular, to our knowledge, 3D Dirac phonons have not been reported in the literature. In analogy to 3D Dirac fermions, a 3D Dirac phonon can be regarded as the overlap of two Weyl phonons with opposite chirality, which is protected by a combination of \mathcal{T} and inversion (\mathcal{P}) symmetries, i.e., the \mathcal{PT} symmetry [28–30]. Around such a phonon Dirac point, the quasiparticle excitations exhibit linear dispersion, which can be described by the massless Dirac equation [31].

In this Letter, we identify that there are 92 space groups with \mathcal{PT} symmetry by screening symmetry conditions. All these space groups are investigated to search for 3D Dirac phonons, which can be classified into two categories. The first category possesses the Dirac points at the high symmetry points (HSPs), and the second category possesses the Dirac points along the high symmetry lines (HSLs). High-throughput calculations were performed to search for candidates of 3D Dirac phonons (see the computational methods in the Supplemental Material [32]). We identify that Si ($c116$) and $\text{Nb}_3\text{Te}_3\text{As}$ are representative candidates for each category, respectively.

To realize 3D Dirac phonons, the fourfold degeneracy of phonon branches is a prerequisite. As is well known, a trivial degeneracy is often fragile due to the unavoidable perturbations [40]. Fortunately, the perturbation term can be rigorously forbidden in crystalline solids. In other words, the phonon branch crossings are protected by specific crystal symmetries, forming nontrivial crossing points. In principle, the fourfold degeneracy can be achieved in either of two forms: (1) the essential degeneracy at the HSPs or (2) the accidental degeneracy along the HSLs. Based on the symmetry analysis and irreducible representations (IRs) in 230 space groups [41], we respectively investigate these two categories of 3D Dirac phonons, and their symmetry constraints are completely identified.

To begin with, we focus on the first category of 3D Dirac phonons at the HSPs. Through checking IRs at the HSPs of 92 centrosymmetric space groups, we reveal 21 HSPs (within 17 space groups) that can host 3D Dirac phonons, as listed in Table S1 of the Supplemental Material [32]. It is worth noting that the cases of the presence of Dirac nodal lines or quadratic dispersion have been excluded (see Table S2 in the Supplemental Material [32]). Further analysis shows that 13 HSPs (within 11 space groups) possess only four-dimensional (4D) IRs (see Table I), and the minimal symmetry condition for the presence of 4D IRs can be described by

$$R_{\alpha(\beta)}^2 = 1, \quad \{R_\alpha, R_\beta\} = 0, \quad \{R_{\alpha(\beta)}, \mathcal{PT}\} = 0, \quad (1)$$

where $R_{\alpha(\beta)}$ represent the nonsymmorphic symmetry operators. Besides these 13 HSPs listed in Table I, another 8 HSPs within 7 space groups given in the bottom panel of Table S1 cannot be explained by Eq. (1), and the corresponding analysis is provided in the Supplemental Material [32].

As a typical example, we illustrate the space group *Ibca* (No. 73), in which 4D IR emerges only at W with the wave vector $\mathbf{k}_W = (1/2, 1/2, 1/2)$. In this case, $R_\alpha = S_{2x}$ and $R_\beta = S_{2y}$ are two screw rotations involving

half lattice translations, which lead to the coordinate transformation as

$$\begin{aligned} S_{2x} : (x, y, z) &\rightarrow (x, -y, -z + 1/2), \\ S_{2y} : (x, y, z) &\rightarrow (-x + 1/2, y, -z). \end{aligned} \quad (2)$$

The symmetry transformation leads to

$$S_{2x}S_{2y} = T_z S_{2y}S_{2x}, \quad (3)$$

where T_z is a unit lattice translation along the z direction. At the W point, this translational operation brings a phase factor on Bloch states as $e^{ik_W \cdot T_z} = -1$, leading to the anticommutation relation $\{S_{2x}, S_{2y}\} = 0$. The other relations in Eq. (1) can be confirmed by employing the same argument.

To determine the dimension of IRs, we start with two groups of Bloch states

$$A : \{|\varphi\rangle, \mathcal{PT}S_{2y}|\varphi\rangle\}, \quad B : \{S_{2y}|\varphi\rangle, \mathcal{PT}|\varphi\rangle\}, \quad (4)$$

where $|\varphi\rangle$ can be chosen as an eigenstate of S_{2x} with $S_{2x}|\varphi\rangle = \pm|\varphi\rangle$, since $S_{2x}^2 = 1$. Then the states in different groups are assigned with opposite S_{2x} eigenvalues according to the anticommutation relations in Eq. (1). This suggests that any state in one group cannot be a linear combination of the states in the other group. Then we focus on the states in the same group, e.g., the group A . We assume that $|\varphi\rangle$ and $\mathcal{PT}S_{2y}|\varphi\rangle$ are linearly dependent, i.e., $|\varphi\rangle = \mu\mathcal{PT}S_{2y}|\varphi\rangle$, where μ is a complex constant. The anticommutation relation $\{S_{2x}, \mathcal{PT}\} = 0$ gives

$$|\varphi\rangle = \mu\mathcal{PT}S_{2y} \cdot \mu\mathcal{PT}S_{2y}|\varphi\rangle = -|\mu|^2|\varphi\rangle, \quad (5)$$

which means that the solution of μ does not exist, and thus $|\varphi\rangle$ and $\mathcal{PT}S_{2y}|\varphi\rangle$ must be linearly independent. A similar argument is also suitable for the group B . As a result, we can conclude that the four states in Eq. (4) are linearly independent and have the same eigenvalue of \hat{H} . These four states can always be constructed into four degenerate complete orthonormal sets of \hat{H} , and thus the IRs are 4D.

Because the nonsymmorphic symmetries may induce a higher degeneracy (i.e., bands-sticking-together effect) [42], the 4D IRs of HSPs are guaranteed to locate at the boundary of the first Brillouin zone (BZ). In addition, due to the \mathcal{T} symmetry, the 4D IRs are the direct sum of a pair of conjugated IRs. For all the HSPs in Table I, the dispersion of phonon branches is linear, forming Dirac phonons. In Fig. 1(a), a representative dispersion of Dirac phonons is plotted to make an intuitive description. Note that the electronic bands of two spin channels degenerate in pairs under the constraint of the \mathcal{PT} symmetry in Dirac semimetals. Nevertheless, spinless phonon branches can individually arise along a general k path, resulting in

TABLE I. Space groups and corresponding high symmetry points (HSPs) that possess Dirac phonons, as well as the key operators that guarantee 4D IRs under the restriction of \mathcal{T} .

Space group (HSP)	$R_{\alpha(\beta)}$
73(W) and 142/206/230(P)	$\{C_{2x} 00\frac{1}{2}\}$ and $\{C_{2y} \frac{1}{2}00\}$
52(S)	$\{C_{2x} 0\frac{1}{2}\frac{1}{2}\}$ and $\{C_{2z} \frac{1}{2}00\}$
54(U) and 54(R)	$\{C_{2y} 00\frac{1}{2}\}$ and $\{C_{2z} \frac{1}{2}00\}$
56(U)	$\{C_{2y} 0\frac{1}{2}\frac{1}{2}\}$ and $\{C_{2z} \frac{1}{2}\frac{1}{2}0\}$
60(T)	$\{C_{2x} \frac{1}{2}\frac{1}{2}0\}$ and $\{C_{2y} 00\frac{1}{2}\}$
56(T) and 130/138(R)	$\{C_{2x} \frac{1}{2}0\frac{1}{2}\}$ and $\{C_{2z} \frac{1}{2}\frac{1}{2}0\}$
228(W)	$\{C_{2x} 0\frac{1}{4}\frac{1}{4}\}$ and $\{C_{2y\bar{z}} \frac{1}{2}\frac{1}{2}\frac{1}{2}\}$

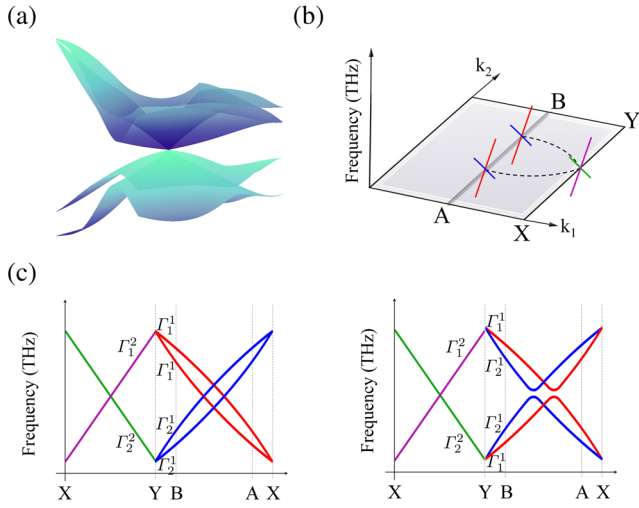


FIG. 1. (a) 3D representation of the Dirac phonon. (b) Sketch of the nodal line induced by accidental degeneracy along the HSL. Red and blue lines indicate Γ_1^1 and Γ_2^1 , which are 1D IRs in the high symmetry plane. Purple and green lines indicate Γ_1^2 and Γ_2^2 , which are 2D IRs along the HSL. (c) Two cases of phonon branch splitting along a close path $A-B$ when a symmetry-protected crossing emerges along $X-Y$.

different behaviors between Dirac phonons and Dirac fermions.

Next, we turn to the second category of Dirac phonons along the HSLs. The Dirac phonons in this category are induced by band inversion. In general, there should be two sets of twofold-degenerate phonon branches crossing each other and completely separated away from the crossing point. If these two sets of phonon branches are assigned to different two-dimensional (2D) IRs, the gapless point is symmetry protected and thus cannot be gapped by local perturbations. Following this rule, we search through all the space groups with inversion symmetry to look for HSLs that possess two or more sets of 2D IRs. The results show that most cases lead to nodal-line phonons in high symmetry planes rather than Dirac phonons along the HSL.

To elaborate on this, we consider the evolution of two sets of 2D IRs Γ_1^2 and Γ_2^2 , which form a symmetry-protected crossing point along the HSL $X-Y$ (see Fig. 1). In addition, we choose an arbitrary path $A-B$ parallel to $X-Y$. These two selected paths lie in a high symmetry plane $k_1 - k_2$ [see Fig. 1(b)]. When $A-B$ is infinitely close to $X-Y$, the phonon dispersion along $A-B$ can be regarded as slight deformations of that along $X-Y$. As a result, the 2D IRs Γ_1^2 and Γ_2^2 along $X-Y$ will split into two one-dimensional (1D) IRs along $A-B$, i.e., Γ_1^1 and Γ_2^1 . According to the compatibility relations, there will be two cases of splitting, either $\Gamma_1^2 = \Gamma_1^1 \oplus \Gamma_1^1$, $\Gamma_2^2 = \Gamma_2^1 \oplus \Gamma_2^1$ or $\Gamma_1^2 = \Gamma_1^1 \oplus \Gamma_2^1$, $\Gamma_2^2 = \Gamma_1^1 \oplus \Gamma_2^1$. We plot these two cases in Fig. 1(c). In the left panel of Fig. 1(c), the crossings along $A-B$ will be preserved. This can happen if the $k_1 - k_2$ plane is a reflection-invariant plane and the crossings along $A-B$

TABLE II. Space groups that host Dirac phonons along the HSLs. The superscripts indicate the dimension of IRs. The symbol “ \oplus ” represents the direct sum of two sets of IRs combined by the T symmetry.

Space group (HSL)	Irreducible representations
62(P/E) and 55/56/58/59(Q)	$\Gamma_1^1 \oplus \Gamma_2^1, \Gamma_3^1 \oplus \Gamma_4^1$
175/176(Δ)	$\Gamma_3^1 \oplus \Gamma_5^1, \Gamma_4^1 \oplus \Gamma_6^1$
191 – 194(Δ)	Γ_5^2, Γ_6^2

are protected by the mirror symmetry. Then, the continuous deformation of $A-B$ will generate two nodal lines in the plane $k_1 - k_2$ [the black dashed lines in Fig. 1(b)] and the 3D Dirac phonons are not allowed. In the right panel of Fig. 1(c), two branches with the same IR are forbidden from forming a crossing. In this case, the 3D Dirac phonons can be present solely along $X-Y$. In Table S3 of the Supplemental Material [32], we tabulate all the centrosymmetric space groups and HSLs with two or more sets of 2D IRs as well as their compatibility relations with the high symmetry planes. We can see that the 3D Dirac phonons along the HSLs are quite limited. The space groups that can host 3D Dirac phonons along the HSLs are summarized in Table II.

Based on the above symmetry analysis, we carry out high-throughput screening of phonon-branch topology to search for these two categories of candidates with 3D Dirac phonons. For Dirac points at the HSPs, the existence of independent 4D IRs implies that any material belonging to the proposed space groups could hold such 3D Dirac phonons. In comparison with the case of Dirac points at the HSPs, the search for 3D Dirac phonons along the HSLs is more difficult because there are only a few space groups that satisfy the symmetry conditions. In addition, it is worth noting that the 3D Dirac phonons may usually be hidden in rambling branches, and thus their topological features are invisible. Fortunately, we find several candidates with visible Dirac phonons. Here we take Si ($cI16$) and $\text{Nb}_3\text{Te}_3\text{As}$ as examples to show 3D Dirac phonons at the HSPs and along the HSLs, respectively. Both materials have been successfully synthesized [43,44], indicating the feasibility in experiments. Other candidates with 3D Dirac phonons are provided in the Supplemental Material [32].

Si ($cI16$) is a silicon allotrope with space group $Ia-3$ (No. 206). It crystallizes in a body-centered cubic structure with 16 atoms in its primitive unit cell, as shown in Fig. 2(a). The first BZ along with the projected (110) surface BZ are given in Fig. 2(b). We first elucidate that there are 4D IRs at point P that is invariant under the operations of $C_{3,111}$ and $S_{2\alpha} = \{C_{2\alpha} | \mathbf{t}_\beta\}$ ($\alpha = x, y, z; \beta = z, x, y$), where $C_{3,111}$ is the threefold rotation along the [111] direction and $S_{2\alpha}$ are the twofold screw rotations along the α direction with half lattice translations \mathbf{t}_β along the β direction. The little group of P satisfies the minimal

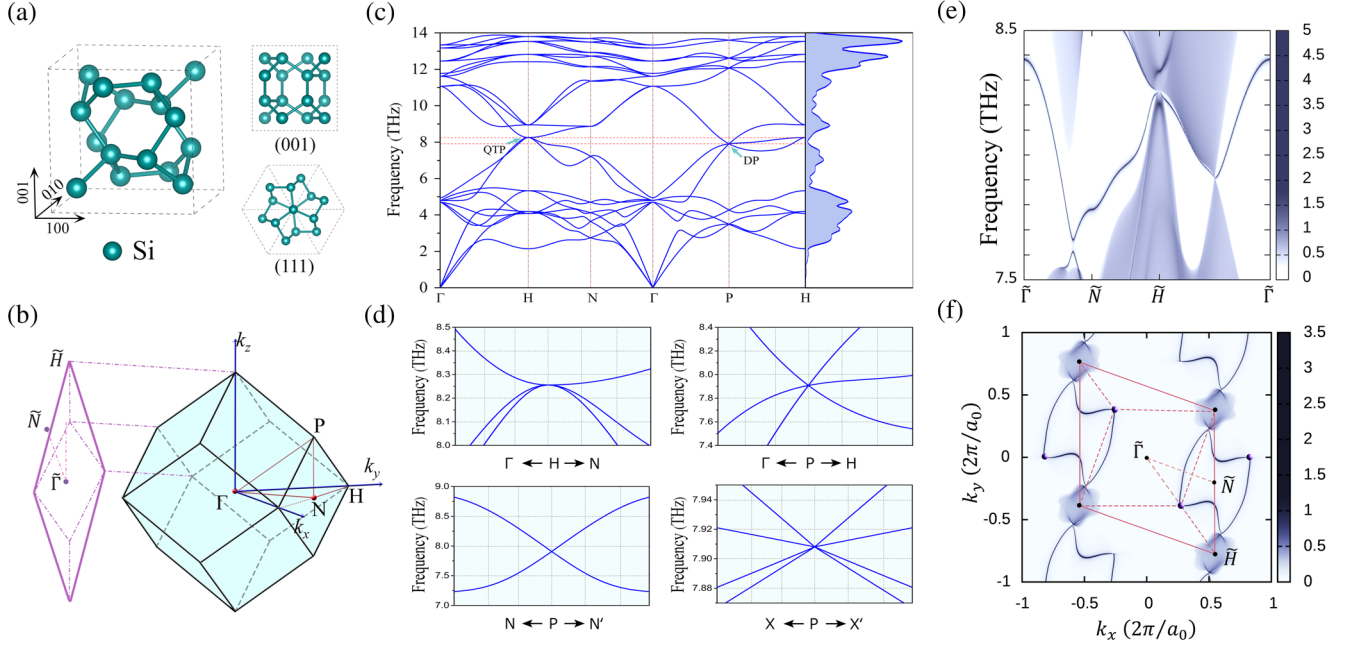


FIG. 2. (a) Side and top views of Si (*cI16*) in the conventional cell. (b) The first BZ of the primitive cell and the (110) surface BZ. (c) Phonon spectrum and density of states. (d) Phonon dispersion of a quadratic triple degenerate point (QTP) and Dirac phonon (DP) along different directions. (e) Phonon surface states and (f) arcs projected on the (110) surface.

symmetry condition of Dirac points at the HSPs in Eq. (1) (see the details in the Supplemental Material [32]). Ignoring the \mathcal{T} symmetry, we can use the eigenvalues of $C_{3,111}$ to represent the IRs as $P_1: \text{diag}(1, e^{i2\pi/3})$, $P_2: \text{diag}(e^{i2\pi/3}, e^{-i2\pi/3})$, and $P_3: \text{diag}(e^{-i2\pi/3}, 1)$. In a phonon system, the complex IRs always appear in pairs, as \mathcal{T} is always conserved. As a consequence, the IRs at P are given as $P' = P_1 \oplus P_3$ and $P'' = P_2 \oplus P_2$, which are both 4D.

The phonon spectrum of Si (*cI16*) along the high symmetry path is shown in Fig. 2(c). As expected, fourfold degeneracies are present at P for all branch nodes. In particular, the linear excitations of Dirac phonons near the frequency of 8 THz are well separated with other phonon branches, facilitating their detection in experiments. To intuitively show the topological features of 3D Dirac phonons in Si (*cI16*), the enlarged views around the Dirac point along several typical paths are shown in Fig. 2(d). We can find that the degenerate behaviors vary along different directions in momentum space. In addition, it is worth noting that there is a quadratic triple degenerate point at H , of which the branches are decoupled along the Γ - H - N path [see Fig. 2(d)], exhibiting the quadratic dispersion.

To obtain topological surface states of Si (*cI16*) at the HSPs, we construct a phonon Wannier tight-binding Hamiltonian using the real-space force constants [45]. The calculated phonon local density of states and the corresponding isofrequency surface projected on the (110) surface of Si (*cI16*) are illustrated in Figs. 2(e) and 2(f), respectively. The surface states are composed of two sets. Each set can be viewed as the surface phonon states of

Weyl phonons because the Dirac points can be treated as the overlap of two Weyl points with opposite chirality. Figure 2(f) clearly shows that the phonon surface arcs cross over the boundary of the first BZ and connect the projections of two nonequivalent Dirac points.

In the following, we show 3D Dirac phonons in $\text{Nb}_3\text{Te}_3\text{As}$ along the HSLs. $\text{Nb}_3\text{Te}_3\text{As}$ crystallizes in a hexagonal structure with space group $P63/m$ (No. 176), as shown in Fig. 3(a). The bulk BZ and (101) surface BZ are shown in Fig. 3(b). The results show that two phonon

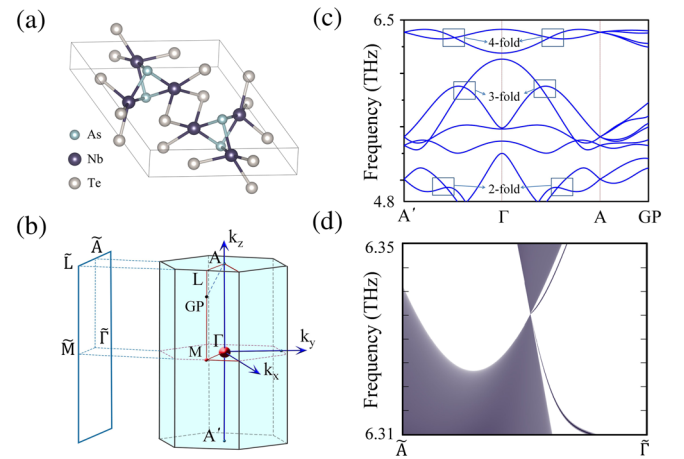


FIG. 3. (a) Side view of $\text{Nb}_3\text{Te}_3\text{As}$. (b) The first BZ and projected surface BZ parallel to the k_z axis. (c) Phonon spectrum of $\text{Nb}_3\text{Te}_3\text{As}$ ranging from 4.8 THz to 6.5 THz. Square boxes indicate the accidental degeneracies along the $A'-\Gamma-A$ path. (d) Phonon surface states near the Dirac phonon.

branches cross along the $A'-\Gamma-A$ path at a frequency of approximately 6.34 THz [see Fig. 3(c)]. Such crossing points are protected by the screw rotation symmetry S_{6z} . There are six 1D IRs, which associate with the eigenvalues of S_{6z} as $E_n = e^{i\pi n/3} \cdot e^{-ik_z c/2}$, where c is the lattice constant and n is an integer ($n \in [0, 5]$). Because of the T symmetry, (E_1, E_5) and (E_2, E_4) respectively become two pairs of complex conjugate representations, leading to two sets of twofold-degenerate phonon branches along $A'-\Gamma-A$. As a result, the Dirac point arising from the crossing between (E_1, E_5) and (E_2, E_4) is present. In addition, twofold and threefold degenerate points can also be found, as 1D IR is allowed on the k_z axis. Figure 3(d) gives the phonon surface states along the projected $\tilde{\Gamma}-\tilde{A}$ path. There are two branches of nontrivial phonon surface states, which are both terminated at the projected Dirac point, exhibiting the unique topological feature.

To summarize, we have investigated the symmetry conditions for the presence of 3D Dirac phonons in systems with inversion symmetry, and two categories of 3D Dirac phonons (i.e., at the HSPs and along the HSLs) are uncovered. The symmetry arguments reveal that the \mathcal{PT} symmetry and nonsymmorphic symmetries play critical roles in the topological classification of 3D Dirac phonons. As a result, all the centrosymmetric space groups that can host 3D Dirac phonons are identified. Furthermore, we provide several realistic materials that realize 3D Dirac phonons. These candidates are expected to be confirmed by experiments such as inelastic neutron scattering, inelastic x-ray scattering, and He atom scattering. Our findings not only offer the complete topological classification of 3D Dirac phonons in crystalline solids, but can also be extended to 3D Dirac bosons in both phononic and photonic systems.

This work is supported by the Guangdong Natural Science Funds for Distinguished Young Scholars (Grant No. 2017B030306008), the National Natural Science Foundation of China (Grants No. 11974160, No. 12074126, and No. 11974062), the Guangdong Provincial Key Laboratory of Computational Science and Material Design (Grant No. 2019B030301001), and the Center for Computational Science and Engineering of Southern University of Science and Technology.

* zhaoyj@scut.edu.cn

† xuh@sustech.edu.cn

- [1] H. Zhang, C.-X. Liu, X.-L. Qi, X. Dai, Z. Fang, and S.-C. Zhang, *Nat. Phys.* **5**, 438 (2009).
- [2] X.-L. Qi and S.-C. Zhang, *Rev. Mod. Phys.* **83**, 1057 (2011).
- [3] X. Wan, A. M. Turner, A. Vishwanath, and S. Y. Savrasov, *Phys. Rev. B* **83**, 205101 (2011).
- [4] Z. Wang, M. G. Vergniory, S. Kushwaha, M. Hirschberger, E. V. Chulkov, A. Ernst, N. P. Ong, R. J. Cava, and B. A. Bernevig, *Phys. Rev. Lett.* **117**, 236401 (2016).
- [5] H. Weng, C. Fang, Z. Fang, B. A. Bernevig, and X. Dai, *Phys. Rev. X* **5**, 011029 (2015).
- [6] Z. Wang, Y. Sun, X.-Q. Chen, C. Franchini, G. Xu, H. Weng, X. Dai, and Z. Fang, *Phys. Rev. B* **85**, 195320 (2012).
- [7] Z. Wang, H. Weng, Q. Wu, X. Dai, and Z. Fang, *Phys. Rev. B* **88**, 125427 (2013).
- [8] S. M. Young, S. Zaheer, J. C. Y. Teo, C. L. Kane, E. J. Mele, and A. M. Rappe, *Phys. Rev. Lett.* **108**, 140405 (2012).
- [9] Q. S. Wu, C. Piveteau, Z. Song, and O. V. Yazyev, *Phys. Rev. B* **98**, 081115(R) (2018).
- [10] Z. Liu, J. Jiang, B. Zhou, Z. Wang, Y. Zhang, H. Weng, D. Prabhakaran, S. Mo, H. Peng, P. Dudin *et al.*, *Nat. Mater.* **13**, 677 (2014).
- [11] M. Neupane, S.-Y. Xu, R. Sankar, N. Alidoust, G. Bian, C. Liu, I. Belopolski, T.-R. Chang, H.-T. Jeng, H. Lin *et al.*, *Nat. Commun.* **5**, 3786 (2014).
- [12] Z. Liu, B. Zhou, Y. Zhang, Z. Wang, H. Weng, D. Prabhakaran, S.-K. Mo, Z. Shen, Z. Fang, X. Dai *et al.*, *Science* **343**, 864 (2014).
- [13] J. Xiong, S. K. Kushwaha, T. Liang, J. W. Krizan, M. Hirschberger, W. Wang, R. J. Cava, and N. P. Ong, *Science* **350**, 413 (2015).
- [14] A. Levine, *Nuovo Cimento* **26**, 190 (1962).
- [15] L. Lu, C. Fang, L. Fu, S. G. Johnson, J. D. Joannopoulos, and M. Soljacic, *Nat. Phys.* **12**, 337 (2016).
- [16] R. A. Sepkhanov, J. Nilsson, and C. W. J. Beenakker, *Phys. Rev. B* **78**, 045122 (2008).
- [17] Z.-G. Chen, X. Ni, Y. Wu, C. He, X.-C. Sun, L.-Y. Zheng, M.-H. Lu, and Y.-F. Chen, *Sci. Rep.* **4**, 4613 (2014).
- [18] F. Liu, Y. Lai, X. Huang, and C. T. Chan, *Phys. Rev. B* **84**, 224113 (2011).
- [19] Y. Li, Y. Wu, and J. Mei, *Appl. Phys. Lett.* **105**, 014107 (2014).
- [20] J. Lu, C. Qiu, S. Xu, Y. Ye, M. Ke, and Z. Liu, *Phys. Rev. B* **89**, 134302 (2014).
- [21] T. Zhang, Z. Song, A. Alexandradinata, H. Weng, C. Fang, L. Lu, and Z. Fang, *Phys. Rev. Lett.* **120**, 016401 (2018).
- [22] J. Li, Q. Xie, S. Ullah, R. Li, H. Ma, D. Li, Y. Li, and X.-Q. Chen, *Phys. Rev. B* **97**, 054305 (2018).
- [23] S. Singh, Q. S. Wu, C. Yue, A. H. Romero, and A. A. Soluyanov, *Phys. Rev. Mater.* **2**, 114204 (2018).
- [24] Y. J. Jin, Z. J. Chen, B. W. Xia, Y. J. Zhao, R. Wang, and H. Xu, *Phys. Rev. B* **98**, 220103(R) (2018).
- [25] Y. Jin, R. Wang, and H. Xu, *Nano Lett.* **18**, 7755 (2018).
- [26] H. Miao, T. T. Zhang, L. Wang, D. Meyers, A. H. Said, Y. L. Wang, Y. G. Shi, H. M. Weng, Z. Fang, and M. P. M. Dean, *Phys. Rev. Lett.* **121**, 035302 (2018).
- [27] T. T. Zhang, H. Miao, Q. Wang, J. Q. Lin, Y. Cao, G. Fabbris, A. H. Said, X. Liu, H. C. Lei, Z. Fang *et al.*, *Phys. Rev. Lett.* **123**, 245302 (2019).
- [28] L. Lu, L. Fu, J. Joannopoulos, and M. Soljacic, in *CLEO: 2013* (Optical Society of America, 2013), pp. 1–2, https://doi.org/10.1364/CLEO_QELS.2013.QTh1A.2.
- [29] N. P. Armitage, E. J. Mele, and A. Vishwanath, *Rev. Mod. Phys.* **90**, 015001 (2018).
- [30] O. Vafek and A. Vishwanath, *Annu. Rev. Condens. Matter Phys.* **5**, 83 (2014).

- [31] J. Mei, Y. Wu, C. T. Chan, and Z.-Q. Zhang, *Phys. Rev. B* **86**, 035141 (2012).
- [32] See Supplemental Material at <http://link.aps.org/supplemental/10.1103/PhysRevLett.126.185301> for more details of symmetry analysis and corresponding materials, which includes Refs. [33–39].
- [33] W. Kohn and L. J. Sham, *Phys. Rev.* **140**, A1133 (1965).
- [34] G. Kresse and J. Furthmüller, *Phys. Rev. B* **54**, 11169 (1996).
- [35] G. Kresse and J. Furthmüller, *Comput. Mater. Sci.* **6**, 15 (1996).
- [36] J. P. Perdew, K. Burke, and M. Ernzerhof, *Phys. Rev. Lett.* **77**, 3865 (1996).
- [37] A. Togo and I. Tanaka, *Scr. Mater.* **108**, 1 (2015).
- [38] M. L. Sancho, J. L. Sancho, J. L. Sancho, and J. Rubio, *J. Phys. F* **15**, 851 (1985).
- [39] L. Elcoro, B. Bradlyn, Z. Wang, M. G. Vergniory, J. Cano, C. Felser, B. A. Bernevig, D. Orobengoa, G. Flor, and M. I. Aroyo, *J. Appl. Crystallogr.* **50**, 1457 (2017).
- [40] J. Von Neumann and E. Wigner, in *The Collected Works of Eugene Paul Wigner. The Collected Works of Eugene Paul Wigner (Part A: The Scientific Papers. Part B: Historical, Philosophical, and Socio-Political Papers)*, edited by A. S. Wightman (Springer, Berlin, Heidelberg, 1993), https://doi.org/10.1007/978-3-662-02781-3_20.
- [41] M. I. Aroyo, A. Kirov, C. Capillas, J. Perez-Mato, and H. Wondratschek, *Acta Crystallogr. Sect. A* **62**, 115 (2006).
- [42] V. Heine, *Group Theory in Quantum Mechanics: An Introduction to Its Present Usage* (Courier Corporation, North Chelmsford, MA, 2007).
- [43] A. Wosylus, H. Rosner, W. Schnelle, and U. Schwarz, *Z. Anorg. Allg. Chem.* **635**, 700 (2009).
- [44] W. Bensch and W. Heid, *J. Alloys Compd.* **224**, 220 (1995).
- [45] Q. Wu, S. Zhang, H.-F. Song, M. Troyer, and A. A. Soluyanov, *Comput. Phys. Commun.* **224**, 405 (2018).